crystals

Article

Study of Multi-Channel Mode-Division Multiplexing Based on a Chalcogenide-Lithium Niobate Platform

Jiacheng Zheng [1,2,3], Bowen Liu [1,2,3], Yuefei Weng [1,2,3] and Baoan Song [1,2,3,*]

1 Faculty of Electrical Engineering and Computer Science, Ningbo University, Ningbo 315211, China
2 Zhejiang Key Laboratory of Photoelectric Materials and Devices, Ningbo 315211, China
3 Engineering Research Center for Advanced Infrared Photoelectric Materials and Devices of Zhejiang Province, Ningbo 315211, China
* Correspondence: songbaoan@nbu.edu.cn

Abstract: A multi-channel mode-division multiplexing based on a chalcogenide-lithium niobate platform using chalcogenide films with adjustable refractive index is proposed, with the aim of overcoming issues with narrow bandwidth and large crosstalk in conventional multiplexers. An asymmetric directional coupler, employing chalcogenide-based thin-film modulation, was designed to realize the multiplexing and separation of TE_1, TE_2, and TE_3 modes. Simulations show that the device is capable of obtaining an insertion loss of between 0.03 dB and 0.7 dB and a crosstalk of between −21.66 dB and −28.71 dB at 1550 nm. The crosstalk of the TE_1, TE_2, and TE_3 modes is below −20.1 dB when accessing the waveguide output port in the 1500–1600 nm band. The proposed multiplexer is a promising approach to enhance the transmission capability of thin-film lithium-niobate-integrated optical paths.

Keywords: chalcogenide films; lithium niobate films; asymmetric directional coupler; mode-division multiplexer

check for updates

Citation: Zheng, J.; Liu, B.; Weng, Y.; Song, B. Study of Multi-Channel Mode-Division Multiplexing Based on a Chalcogenide-Lithium Niobate Platform. *Crystals* **2024**, *14*, 73. https://doi.org/10.3390/cryst14010073

Academic Editors: Tzi-yi Wu, Ali Belarouci and Regis Orobtchouk

Received: 4 December 2023
Revised: 9 January 2024
Accepted: 9 January 2024
Published: 11 January 2024

Copyright: © 2024 by the authors. Licensee MDPI, Basel, Switzerland. This article is an open access article distributed under the terms and conditions of the Creative Commons Attribution (CC BY) license (https://creativecommons.org/licenses/by/4.0/).

1. Introduction

With the continuous development of Internet technology, there has been a rapidly growing demand for transmission capacity in communication systems over the past three decades [1–3]. To meet this growing demand for data, modern data centers and integrated communication systems are increasingly adopting optical interconnect technologies that prioritize energy efficiency to transmit and process optical signals in a compact footprint without compromising key performance metrics, such as propagation loss, tunability, and low crosstalk [4,5]. Optical interconnect systems typically consist of basic components such as lasers, electro-optical modulators, optical multiplexers and photodetectors [6]. Researchers have conducted studies of active and passive optical devices on a variety of platforms, including silicon on insulator (SOI), silicon nitride (SiN), indium phosphate (InP), and lithium niobate on insulator (LNOI) platforms [7–10]. LNOI platforms demonstrate great potential as photonic integrated circuit (PIC) platforms due to their strong electro-optical coefficients and low absorption loss [11–13]. The integration of lithium niobate (LN) in insulators to realize high-speed electro-optic modulators and optical nonlinear devices using a crystal ion slicing technique has attracted extensive research interest [14–20]. To fully realize the potential of LNOI as a platform for PICs, developing passive devices to enable monolithic integration with active devices is essential [21,22]. Nonetheless, there are some challenges associated with direct etching on the LNOI platform, such as limited etching depth and waveguide sidewall tilting [23]. As a result, the LNOI platform also lacks some key passive PIC components that have been demonstrated in other PIC platforms [6]. Among these, chalcogenide glasses (ChGs) with similar refractive indices can be introduced into the lithium niobate platform as an advantageous solution to avoid the above problems.

In recent years, significant research has been conducted on passive PIC components based on lithium niobate platforms [24]. For example, Han et al. designed and performed experiments on a grating coupler for efficient coupling between a single-mode fiber and a silicon nitride-loaded LNOI waveguide [25]. Heterogeneous integrated band-loaded waveguides with amorphous silicon and lithium niobate films developed by Yiwen Wang et al. [26]. In 2020, Yu et al. experimented with a four-channel TM mode (de)multiplexer by utilizing bound states in the continuum (BIC) on a polymer-loaded LNOI platform [27]. However, this BIC waveguide can only direct light of a specific polarization and wavelength and has a high insertion loss. On the other hand, Liu et al. demonstrated a quad-mode (de)multiplexer with a TE mode based on a a silicon rich nitride (SRN)-loaded LNOI platform [23], which had a good performance. Nevertheless, the narrow material bandgap of SRN materials limits the shortest wavelength at which the waveguide can be used. Additionally, there is significant crosstalk in the broadband range, and the effect on fabrication tolerances has not been analyzed in detail. The structure is capable of operating over a wider spectral range, given the wide transparency window and high nonlinear properties of the chalcogenide film [16,28], as well as the lithium niobate platform's superior optical properties and wide bandgap [29]. In addition, the material is less sensitive to fabrication deviations than other materials and is able to maintain stable performance [30]. Evidently, the development of chalcogenide-lithium niobate platforms offers an open and promising research area with the potential for the flexible integration of CMOS-compatible fabrication processes and driver circuits that can play an important role in the related field of photonics, which contributes to exploring high-performance devices such as on-chip high-speed opto-electronic modulators, high-efficiency acousto-optic modulators, high-sensitivity sensors, and coordinable lasers. Hence, there is an urgent need to develop a high-tolerance, wide-bandwidth, and low-crosstalk multiplexer based on a chalcogenide thin-film-composite lithium niobate platform.

A solution is proposed for a high-tolerance, wide-bandwidth, and low-crosstalk multimode multiplexer based on a chalcogenide thin-film composite lithium niobate platform. This study aims to achieve low-crosstalk mode-division multiplexing over a wide bandwidth of 100 nm, provide detailed design principles, present an analysis of fabrication tolerance results, and discuss the practical applications of this scheme. The second part of the article focuses on the construction of a theoretical model and the optimized design of a multimode mode division multiplexer structure, elaborating on the design principles of the proposed solution. In the third part, we thoroughly analyze and discuss the results of the design scheme and manufacturing tolerance, thus offering reliable technical support for the practical application of the proposed solution. Finally, the fourth section summarizes research findings and explores potential future research directions and applications.

2. Theoretical Models

In order to achieve the mode demultiplexing of TE_1, TE_2, and TE_3, the phase matching condition must be satisfied for selectively coupling different higher-order modes [31]. For coupling between two waveguides, assuming that light is input from port 1 with an initial optical field of $A(0) = A_0$ and $B(0) = 0$, the optical power transmitted to the z-point in waveguides 1 and 2, respectively, can be expressed as follows:

$$P_1(z) = \frac{|A(z)|^2}{|A_0|^2} = 1 - F\sin^2(qz) \tag{1}$$

$$P_2(z) = \frac{|A(z)|^2}{|A_0|^2} = F\sin^2(qz) \tag{2}$$

where:

$$\mathrm{q} = \sqrt{k^2 + \delta^2} \tag{3}$$

$$\delta = (\beta_2 - \beta_1)/2 \tag{4}$$

β_1, β_2 represent propagation constants, k is the coupling coefficient, and F is defined as the optimal power coupling efficiency, which is expressed as:

$$F = \frac{1}{1 + \alpha \left| n_{eff1} - n_{eff2} \right|} \tag{5}$$

The mode coupling efficiency $K(z)$ can be written as:

$$K(z) = F \sin(\theta) \tag{6}$$

in which $\theta = \varepsilon z$, α, and ε are constants determined by the structure of the coupled part, the material, and the operating wavelength. n_{eff1} and n_{eff2} are the effective refractive indices of the modes to be coupled. Full power conversion from one mode to another is possible only when $n_{eff1} = n_{eff2}$, which is known as the phase matching condition. Based on Equation (5), the mode coupling per unit length is given by the following equation:

$$\frac{dK(z)}{dz} = \frac{F}{\varepsilon} \cos(\theta) \tag{7}$$

For a tapered asymmetric directional coupler (ADC), F and ε are functions with respect to the propagation distance z. Therefore, the coupling efficiency of a tapered ADC can be expressed as an integral of the propagation distance z:

$$K(L) = \int_0^L \frac{F(z)}{\varepsilon(z)} \cos\theta(z) dz \tag{8}$$

$$\theta(L) = \int_0^L \varepsilon(z) dz \tag{9}$$

According to Equations (8) and (9), the mode coupling efficiency mainly depends on two factors, $F(z)$ and $\varepsilon(z)$, mapped to the geometric parameters of the tapered ADC.

According to the coupled-mode theory, optical energy is periodically coupled between the access waveguide and the bus waveguide. The transmission distance at which the energy in one waveguide can be completely transferred to the other waveguide is defined as the coupling length L_0 [32]:

$$L_0 = \frac{\mu\lambda}{2(n_{eff2} - n_{eff1})} \tag{10}$$

Here, L_0 denotes the minimum coupling length, and μ is a coefficient related to the device structure. Typically, during the first cycle, light is coupled from the access waveguide to the bus waveguide, allowing for a more compact device footprint.

Multi-Channel Pattern Demultiplexer Design and Optimization

A mode-division multiplexer based on a ChG-LN hybrid platform was designed, as shown in Figure 1. Figure 1a shows a cross-section of the device structure, where a lithium niobate (LN) film (from NANOLN) with a thickness of 700 nm is covered with a 370 nm thick $Ge_{20}Sb_{15}Se_{65}$ film (plasma-enhanced chemical vapor deposition) to confine the optical modes in the longitudinal direction (n = 2.66@1550 nm). Electron beam lithography (eLINE Plus, Raith, Dortmund, Germany) and a plasma etching system (Plasmapro100Cobra180, Oxford Instruments, Oxford, UK) were used to prepare a multiplexed mode division multiplexer. Figure 1c shows a three-dimensional schematic of the proposed multichannel mode demultiplexer for multiplexing four modes (TE_0, TE_1, TE_2, TE_3) of a multimode main waveguide. The proposed multiplexer consists of three coupling sections and three adiabatic cones of increasing width in the trunk waveguide [32]. The inset in Figure 1b provides a localized enlarged view of the conical ADC, consisting of a narrow waveguide and a wide conical waveguide, where the narrow waveguide (waveguide width $W1$) is parallel to a tapered waveguide (increasing from *W*2 to *W*4 with a center width of *W*3) that gradually increases in width.

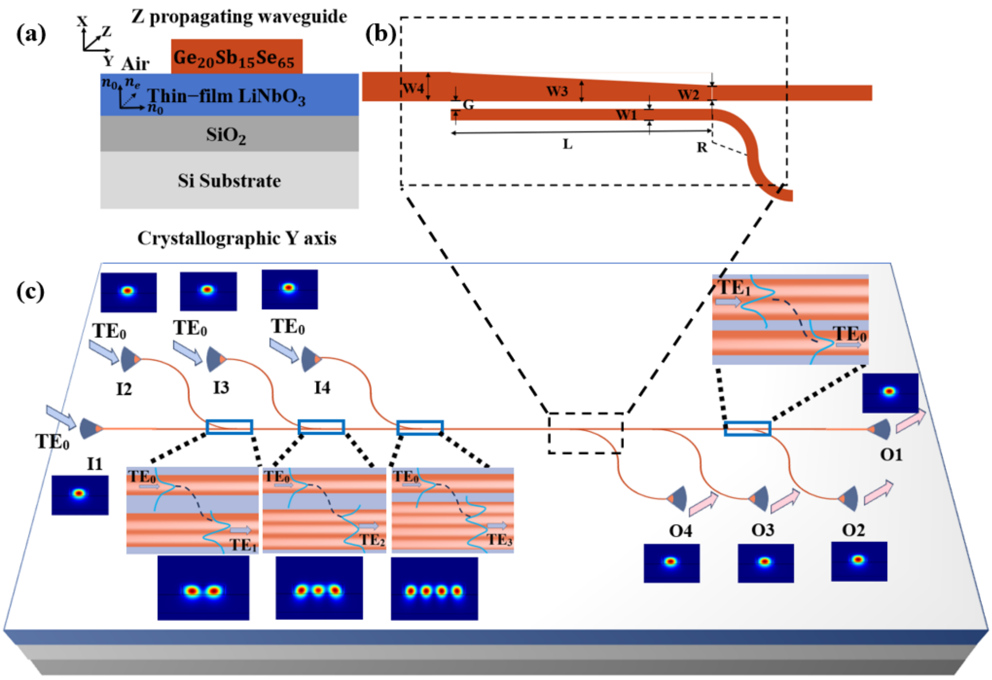

Figure 1. (**a**) Waveguide structure on the ChG-LN hybrid platform. (**b**) Enlarged view of the tapered ADC. (**c**) Schematic of the proposed four-mode (de)multiplexer.

The width of the single-mode waveguide is set to 0.81 µm. Figure 2a,b illustrates the S-shaped waveguide connecting the input waveguide to the multimode waveguide as a function of the waveguide bending radius and loss, with the waveguide bending radius (R) set to 40 µm to ensure negligible bending loss [33,34]. Therefore, the available design parameters are the center width (*W*3) of the tapered waveguide, the taper width difference ($\Delta W = W4 - W2$), and the coupling length (L).

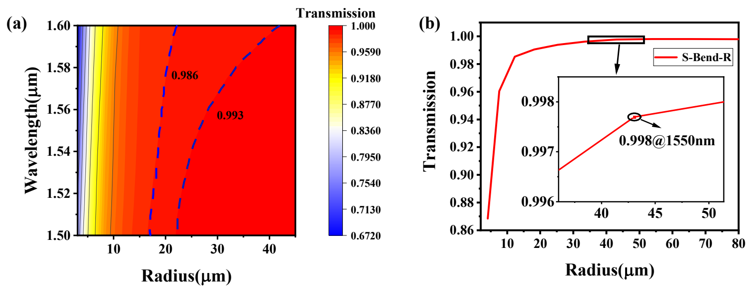

Figure 2. S-bend bending loss versus bending radius R. (**a**) Transmission in the wavelength range of 1500–1600 nm. (**b**) Transmission spectrum at 1500 nm.

Based on the phase matching condition, the width (*W*3) of the multimode waveguide is determined. The effective refractive index of the guiding modes is obtained by calculating the effective refractive index of the modes as shown in Figure 3. The effective refractive index of the modes varies with the geometry of the waveguide. Waveguide phase match points are intersections where different optical modes have the same effective refractive index. In the multimode multiplexer operating at 1550 nm wavelength, the TE_0 mode of the 0.81 µm wide narrow waveguide matches the TE_1 mode of the 1.72 µm wide waveguide, the TE_2 mode of the 2.6 µm wide waveguide, and the TE_3 mode of the 3.52 µm wide waveguide.

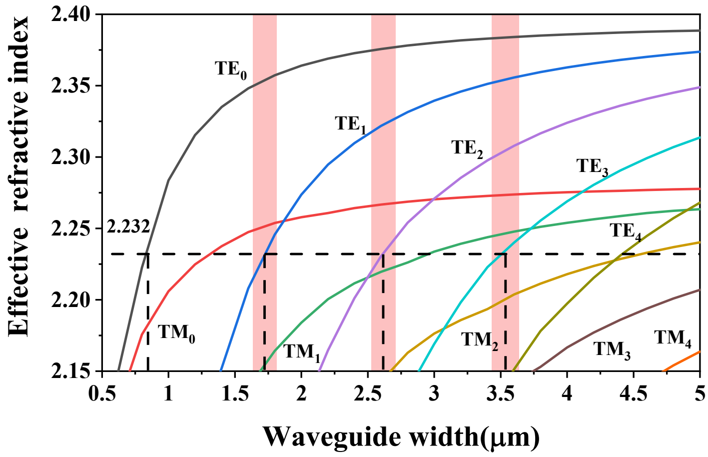

Figure 3. Effective refractive index as a function of waveguide width.

A high mode coupling efficiency is obtained by optimizing the parameters $F(z)$ and $\varepsilon(z)$, which vary with the tapered ADC geometry and are related to $F(W_L)$ and $\varepsilon(W_L)$. The width of the multimode waveguide (W_L) is given by $W_L = W3 - \Delta W/2 + \Delta W/L \times z$.

The $F(W_L)$ and $\varepsilon(W_L)$ values of the multiplexer were obtained through 3D simulation of the non-tapered ADC, as shown in Figure 4. For $F(W_L)$, TE_1, TE_2, and TE_3 can be mode multiplexed in the waveguide width range of 1.4–3.6 μm by injecting TE_0 excitation light into different regions of the multimode waveguide with varying waveguide widths. To suppress higher-order mode crosstalk in the multiplexer, we limited the taper width difference (ΔW) to an appropriate range. By optimizing the design, the best $\Delta W1$ and $\Delta W2$ values were found to be 160 nm, while $\Delta W3$ was 180 nm. Under these conditions, the $F(W_L)$ of TE_0-TE_2 was lower than that of TE_0-TE_1, and the $F(W_L)$ of TE_0-TE_3 was lower than that of TE_0-TE_2. Figure 4 shows that $\varepsilon(W_L)$ is around $W3$ when ΔW is 200 nm, indicating that the minimum value of ε and the phase-matching condition are reached simultaneously.

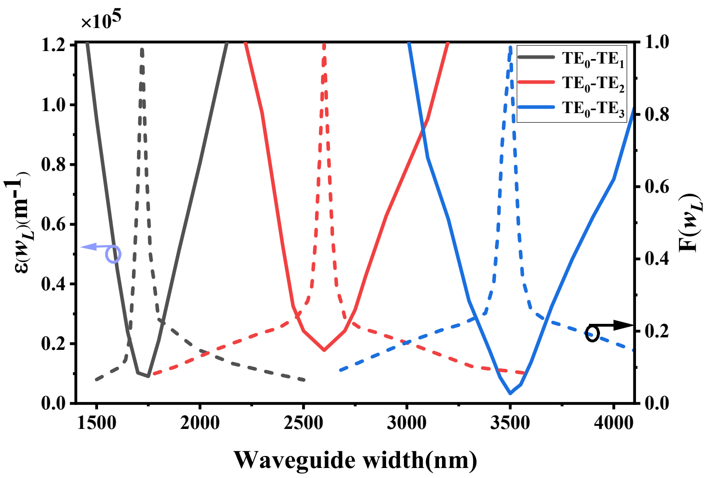

Figure 4. $F(W_L)$ as a function of multimode waveguide width for several modes in the multiplexer and variation in different $\varepsilon(W_L)$ with the multimode waveguide width.

After determining the center width and width difference of the multimode waveguide, the effect of the coupling length on the overall coupling efficiency becomes important. Based on the results obtained from the Eigenmode Expansion Method (EME) numerical calculations, Figure 5 shows the corresponding coupling lengths of 69 μm, 77 μm, and 87 μm for the three tapered ADCs [19]. Table 1 lists the main parameters of the three-part tapered ADC that were applied to the proposed (de)multiplexer.

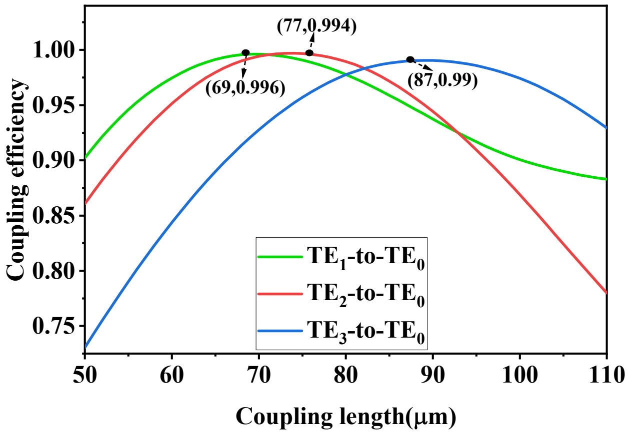

Figure 5. Relationship between coupling length and coupling efficiency for the three modes calculated by EME.

Table 1. Parameters of the optimized tapered ADC.

Mode Order	W1 (nm)	W2 (μm)	W3 (μm)	W4 (μm)	L (μm)	G (nm)
TE_0	810	-	-	-	-	-
TE_1	810	1.64	1.72	1.80	69	170
TE_2	810	2.52	2.60	2.68	77	160
TE_3	810	3.43	3.52	3.61	87	170

3. Results and Discussion

Based on reference [35], the performance of MMUX was evaluated based on mode conversion efficiency (*MCE*), excess loss (*EL*), extinction ratio (*ER*) and crosstalk (*CT*), which can be rewritten as follows:

$$MCE = 10 * \log_{10} \frac{P_{out}}{P_{in}} \tag{11}$$

$$EL = -10 * \log_{10} \frac{P_{out2}}{P_{in}} \tag{12}$$

$$ER = 10 * \log_{10} \frac{P_{out}}{P_{out2}} \tag{13}$$

$$CT = 10 * \log_{10} \frac{P_{out2}}{P_{in}} \tag{14}$$

where P_{out} represents the power of the desired output mode and P_{in} represents the power of the input mode. In addition, P_{out2} is the power of the undesired output mode.

As shown in Figure 6b,d,f, at the design wavelength of 1550 nm, the first-order, second-order, and third-order modes in the multimode waveguide are excited when the light is input to the I2, I3, and I4 ports of the four-channel mode multiplexer from the upper left. The results show that the design mode multiplexer has low crosstalk. Based on the numerical calculations, the normalized transmission spectra of the simulation results for mode conversion in the range of wavelengths from 1500 nm to 1600 nm are analyzed, and the spectral response when the fundamental mode is fed into the port is shown in Figure 6a,c,e. The results show that the mode coupling efficiencies for the TE_0-TE_1, TE_0-TE_2, and TE_0-TE_3 modes are over 99%, and the *MCE* reaches -0.017 dB (>-0.43 dB), -0.035 dB (>-0.43 dB), and -0.043 dB (>-0.85 dB) (across the entire 100 nm wavelength range). At the output port of the access waveguide, the IL of the TE_1, TE_2, and TE_3 modes in the 1500–1600 nm band is less than 0.86 dB, and the *ER* exceeds 27.31 dB. The *CT* for the TE_1, TE_2, and TE_3 modes in the 100 nm band are lower than -35.2 dB, -29.7 dB, and -28.2 dB, respectively. The device is well-suited for wide-bandwidth, low-crosstalk pattern multiplexing or pattern demultiplexing.

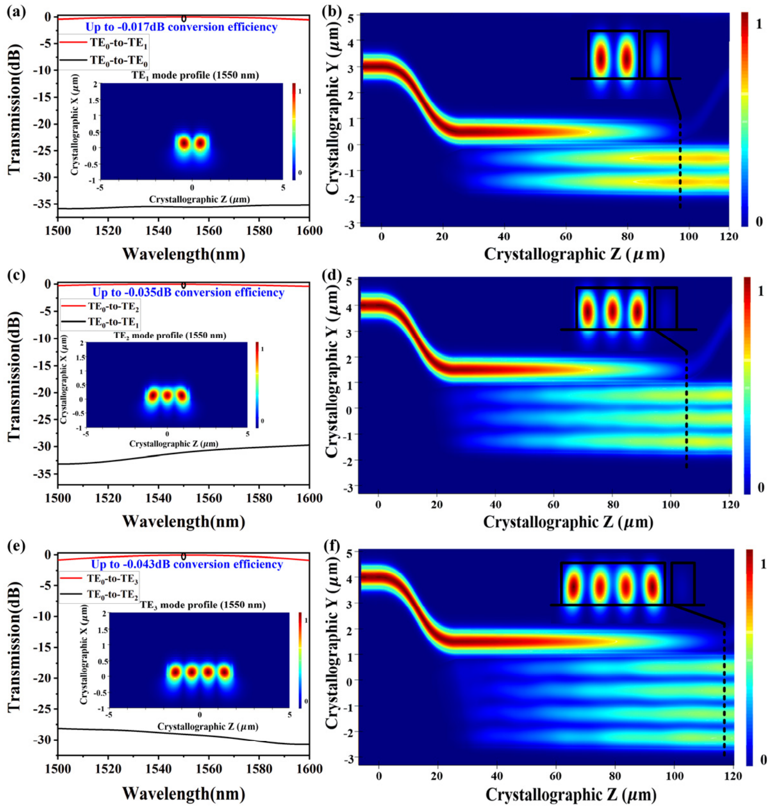

Figure 6. Simulated (**a**–**c**) normalized transmission spectra of TE_0-to-TE_1, TE_0-to-TE_2, and TE_0-to-TE_3 mode transitions, and detected higher-order mode distributions and electric field distributions (**d**–**f**).

Since the difference between the effective refractive index of the TE_1 mode and that of the TM mode is relatively large, the insertion loss of the TE_1 mode is smaller than that of the TE_2 and TE_3 modes. The effective refractive index difference between the TE_2 and TE_3 modes and the TM mode is small, thus leading to mode crosstalk and some insertion loss.

The effects of the chalcogenide waveguide gap G and waveguide width *W* in the deviation range of plus or minus 20 nm, respectively, on the performance of the device are analyzed using time-domain finite-difference calculations, and the spectral response is obtained. As shown in Figure 7a–d, the error in the waveguide coupling gap affects performance metrics such as waveguide mode conversion efficiency and *CT*. The *MCE* of the TE mode is as high as −0.09 dB (98%) or more at 1550 nm and maintains an *MCE* > −0.46 dB (90%) over a bandwidth of about 80 nm. It is also observed that the *CT* of the TE_0-TE_1 mode is able to achieve a level of about −28 dB or less in the 100 nm bandwidth range, while the *CT* of the TE_0-TE_2 modes and the TE_0-TE_3 modes can reach a level of −25 dB or less.

The results of the width variation (Δw) in the range of ±20 nm are shown in Figure 8a–d, while maintaining *MCE* > −0.46 dB (90%) with a deviation from the trend and a sudden increase at Δw = +20 nm for the TE_2 mode. This phenomenon can be attributed to the unequal coupling length at this width compared to the length of the selected straight waveguide. As the width deviation increases, the phase mismatch between the TE_0 mode of the narrow waveguide and the TE_1 and TE_2 modes of the wide waveguide increases, causing a sharp decrease in the *MCE* of the TE mode. This width error achieves an *MCE* above −0.7 dB at 1550 nm and maintains an *MCE* > −0.75 dB over a bandwidth of about 80 nm. Moreover, the *CT* mode is able to reach levels below about −28 dB in the 100 nm bandwidth range.

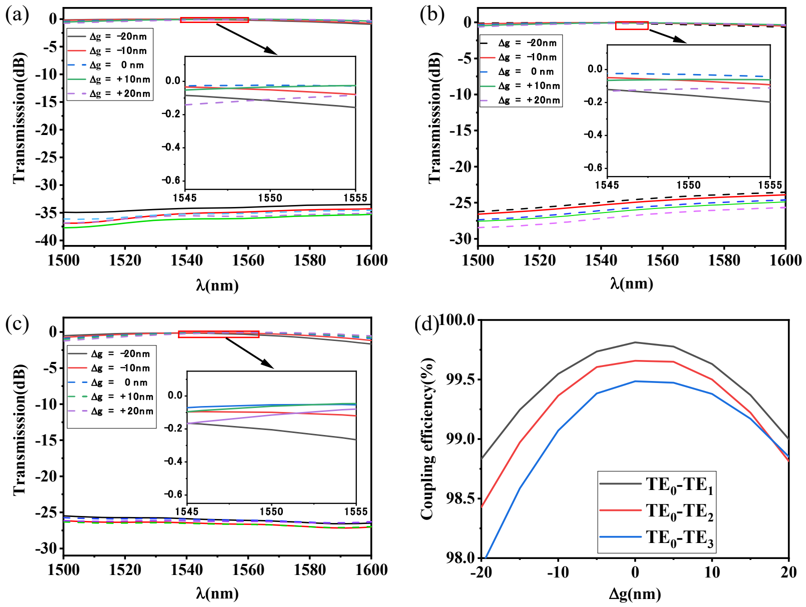

Figure 7. Considering the error of the waveguide coupling gap. (**a**–**c**) Transmission response of the TE_1, TE_2, and TE_3 mode channels; (**d**) coupling efficiency.

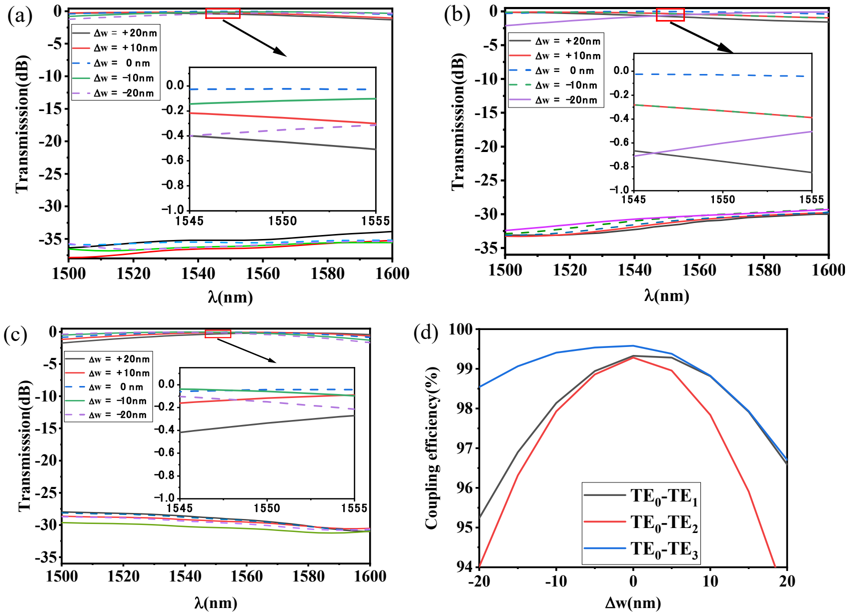

Figure 8. (**a**–**c**) Transmission response of TE_1, TE_2, and TE_3 mode channels and (**d**) coupling efficiency considering the error in waveguide width.

Figure 9 illustrates the corresponding spectral response of the four-channel mode (de)multiplexer by connecting the fundamental mode of the input waveguide to the I1, I2, I3, and I4 ports of the multiplexer, respectively. The demultiplexed crosstalk is lower than −21 dB in the range from 1500 nm to 1600 nm. The main factors limiting the reduction in crosstalk after demultiplexing are the mode coupling between the fundamental mode of I2 and the first-order modes of O2, as well as the mode coupling between the fundamental mode of I4 and the second-order modes of O3. Fabrication tolerances can be indirectly reflected in the wavelength sensitivity of the device. Higher wavelength independence may indicate a device with large fabrication tolerances.

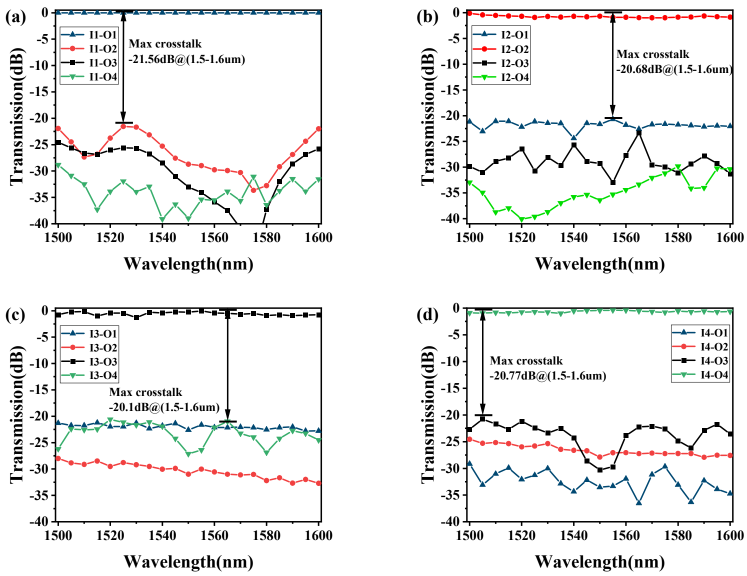

Figure 9. Wavelength dependence of the four-channel mode (demultiplexer). The triangular, circular, rectangular, and inverted triangular curves indicate the signals transmitted by the quad-channel mode multiplexer from ports (**a**–**d**) I1, I2, I3, and I4.

A comparative analysis of the simulated performance of multimode multiplexers reported on the LNOI platform was conducted, and the device parameters are listed in Table 2. The results demonstrate that the multimode multiplexer designed in this study, utilizing a chalcogenide composite LNOI platform, exhibits several advantages, including easy fabrication, low insertion loss, and low crosstalk.

Table 2. Performance of reported mode (de)multiplexers in the LNOI platform.

Ref.	Etching of LN	BIC	Mode Number	Maximum Insertion Loss (1550 nm)	Maximum Crosstalk (1550 nm)	Fabrication Tolerance
[21]	Yes	No	2	/	/	/
[23]	No	No	4	0.18 dB	/	/
[27]	No	Yes	4	0.45 dB	−17.70 dB	/
[36]	No	No	2	/	/	±10 nm
[37]	No	No	3	1.80 dB	−24.00 dB	±20 nm
[6]	No	No	4	0.62 dB	−13.38 dB	/
This study	No	No	4	0.68 dB	−21.65 dB	±20 nm

4. Conclusions

A multimode-division multiplexing device was designed and developed based on an X-cut LNOI platform with chalcogenide thin-film loads. The mode characteristics of the device were numerically simulated and analyzed. The results demonstrate that the device exhibits wide bandwidth characteristics and low crosstalk. The multimode multiplexer achieves an insertion loss of less than 0.1 dB and a crosstalk of less than −20.1 dB for all mode channels in the 1550–1600 nm band. Specifically, at 1550 nm, the entire mode-division-multiplexing system, as well as the TE_1, TE_2, and TE_3 modes, achieves an insertion loss of less than 0.7 dB, and has a fabrication tolerance of 40 nm. This research will lay solid theoretical foundations and provide practical support for high-tolerance, high-capacity optical interconnected technology based on the LNOI platform.

Author Contributions: B.S. conceived the original idea; J.Z. carried out the simulations, analyzed the data, and wrote the paper; B.L. and Y.W. contributed the useful and deep discussions and modified the manuscript. All authors have read and agreed to the published version of the manuscript.

Funding: National Natural Science Foundation of China (62075109, 62135011) and K. C. Wong Magna Fund in Ningbo University.

Data Availability Statement: For privacy reasons, the data presented in this study are available on request from the corresponding author.

Conflicts of Interest: The authors declare no conflicts of interest.

References

1. Zhang, W.; Ghorbani, H.; Shao, T.; Yao, J. On-Chip 4 × 10 GBaud/s Mode-Division Multiplexed PAM-4 Signal Transmission. *IEEE J. Sel. Top. Quantum Electron.* **2020**, *26*, 1–8. [CrossRef]
2. Wang, J.; Long, Y. On-chip silicon photonic signaling and processing: A review. *Sci. Bull.* **2018**, *63*, 1267–1310. [CrossRef] [PubMed]
3. Paredes, B.; Mohammed, Z.; Villegas, J.; Rasras, M. Dual-band (O & C-bands) two-mode multiplexer on the SOI platform. *IEEE Photonics J.* **2021**, *13*, 6600309.
4. Rumley, S.; Bahadori, M.; Polster, R.; Hammond, S.D.; Calhoun, D.M.; Wen, K.; Rodrigues, A.; Bergman, K. Optical interconnects for extreme scale computing systems. *Parallel Comput.* **2017**, *64*, 65–80. [CrossRef]
5. Dai, D.; Li, C.; Wang, S.; Wu, H.; Shi, Y.; Wu, Z.; Gao, S.; Dai, T.; Yu, H.; Tsang, H.K. 10-Channel Mode (de) multiplexer with dual polarizations. *Laser Photonics Rev.* **2018**, *12*, 1700109. [CrossRef]
6. Han, X.; Jiang, Y.; Frigg, A.; Xiao, H.; Zhang, P.; Nguyen, T.G.; Boes, A.; Yang, J.; Ren, G.; Su, Y. Mode and polarization-division multiplexing based on silicon nitride loaded lithium niobate on insulator platform. *Laser Photonics Rev.* **2022**, *16*, 2100529. [CrossRef]
7. Yang, Z.; Wen, M.; Wan, L.; Feng, T.; Zhou, W.; Liu, D.; Zeng, S.; Yang, S.; Li, Z. Efficient acousto-optic modulation using a microring resonator on a thin-film lithium niobate–chalcogenide hybrid platform. *Opt. Lett.* **2022**, *47*, 3808–3811. [CrossRef]
8. Stabile, R. Towards large-scale fast reprogrammable SOA-based photonic integrated switch circuits. *Appl. Sci.* **2017**, *7*, 920. [CrossRef]
9. Chen, W.; Wang, P.; Yang, T.; Wang, G.; Dai, T.; Zhang, Y.; Zhou, L.; Jiang, X.; Yang, J. Silicon three-mode (de) multiplexer based on cascaded asymmetric Y junctions. *Opt. Lett.* **2016**, *41*, 2851–2854. [CrossRef]
10. Blumenthal, D.J.; Heideman, R.; Geuzebroek, D.; Leinse, A.; Roeloffzen, C. Silicon nitride in silicon photonics. *Proc. IEEE* **2018**, *106*, 2209–2231. [CrossRef]
11. Sun, D.; Zhang, Y.; Wang, D.; Song, W.; Liu, X.; Pang, J.; Geng, D.; Sang, Y.; Liu, H. Microstructure and domain engineering of lithium niobate crystal films for integrated photonic applications. *Light Sci. Appl.* **2020**, *9*, 197. [CrossRef] [PubMed]
12. Chang, L.; Pfeiffer, M.H.; Volet, N.; Zervas, M.; Peters, J.D.; Manganelli, C.L.; Stanton, E.J.; Li, Y.; Kippenberg, T.J.; Bowers, J.E. Heterogeneous integration of lithium niobate and silicon nitride waveguides for wafer-scale photonic integrated circuits on silicon. *Opt. Lett.* **2017**, *42*, 803–806. [CrossRef] [PubMed]
13. Boes, A.; Corcoran, B.; Chang, L.; Bowers, J.; Mitchell, A. Status and potential of lithium niobate on insulator (LNOI) for photonic integrated circuits. *Laser Photonics Rev.* **2018**, *12*, 1700256. [CrossRef]
14. Zhu, D.; Shao, L.; Yu, M.; Cheng, R.; Desiatov, B.; Xin, C.; Hu, Y.; Holzgrafe, J.; Ghosh, S.; Shams-Ansari, A. Integrated photonics on thin-film lithium niobate. *Adv. Opt. Photonics* **2021**, *13*, 242–352. [CrossRef]
15. Xu, M.; He, M.; Zhang, H.; Jian, J.; Pan, Y.; Liu, X.; Chen, L.; Meng, X.; Chen, H.; Li, Z. High-performance coherent optical modulators based on thin-film lithium niobate platform. *Nat. Commun.* **2020**, *11*, 3911. [CrossRef] [PubMed]
16. Rao, A.; Patil, A.; Chiles, J.; Malinowski, M.; Novak, S.; Richardson, K.; Rabiei, P.; Fathpour, S. Heterogeneous microring and Mach-Zehnder modulators based on lithium niobate and chalcogenide glasses on silicon. *Opt. Express* **2015**, *23*, 22746–22752. [CrossRef]
17. Qi, Y.; Li, Y. Integrated lithium niobate photonics. *Nanophotonics* **2020**, *9*, 1287–1320. [CrossRef]
18. Poberaj, G.; Hu, H.; Sohler, W.; Guenter, P. Lithium niobate on insulator (LNOI) for micro-photonic devices. *Laser Photonics Rev.* **2012**, *6*, 488–503. [CrossRef]
19. Lin, J.; Bo, F.; Cheng, Y.; Xu, J. Advances in on-chip photonic devices based on lithium niobate on insulator. *Photonics Res.* **2020**, *8*, 1910–1936. [CrossRef]
20. Kharel, P.; Reimer, C.; Luke, K.; He, L.; Zhang, M. Breaking voltage–bandwidth limits in integrated lithium niobate modulators using micro-structured electrodes. *Optica* **2021**, *8*, 357–363. [CrossRef]
21. Zhang, M.; Chen, K.; Wang, M.; Wu, J.; Chiang, K.S. Electro-optic reconfigurable two-mode (de) multiplexer on thin-film lithium niobate. *Opt. Lett.* **2021**, *46*, 1001–1004. [CrossRef]
22. Li, C.; Liu, D.; Dai, D. Multimode silicon photonics. *Nanophotonics* **2019**, *8*, 227–247. [CrossRef]
23. Liu, Y.; Huang, X.; Li, Z.; Guan, H.; Yu, Z.; Wei, Q.; Fan, Z.; Han, W.; Li, Z. On-chip four-mode (de-) multiplexer on thin film lithium niobate–silicon rich nitride hybrid platform. *Opt. Lett.* **2021**, *46*, 3179–3182. [CrossRef] [PubMed]

24. Rabiei, P.; Ma, J.; Khan, S.; Chiles, J.; Fathpour, S. Heterogeneous lithium niobate photonics on silicon substrates. *Opt. Express* **2013**, *21*, 25573–25581. [CrossRef] [PubMed]
25. Han, X.; Jiang, Y.; Frigg, A.; Xiao, H.; Zhang, P.; Boes, A.; Nguyen, T.G.; Yang, J.; Ren, G.; Su, Y.; et al. Single-step etched grating couplers for silicon nitride loaded lithium niobate on insulator platform. *APL Photonics* **2021**, *6*, 086108. [CrossRef]
26. Wang, Y.; Chen, Z.; Cai, L.; Jiang, Y.-Q.; Zhu, H.; Hu, H. Amorphous silicon-lithium niobate thin film strip-loaded waveguides. *Opt. Mater. Express* **2017**, *7*, 4018–4028. [CrossRef]
27. Yu, Z.; Tong, Y.; Tsang, H.K.; Sun, X. High-dimensional communication on etchless lithium niobate platform with photonic bound states in the continuum. *Nat. Commun.* **2020**, *11*, 2602. [CrossRef] [PubMed]
28. Li, J.; Shen, X.; Sun, J.; Vu, K.; Choi, D.-Y.; Wang, R.; Luther-Davies, B.; Dai, S.; Xu, T.; Nie, Q. Fabrication and characterization of Ge20Sb15Se65 chalcogenide glass rib waveguides for telecommunication wavelengths. *Thin Solid Film.* **2013**, *545*, 462–465. [CrossRef]
29. Kaushalram, A.; Talabattula, S. Zero-birefringence dual mode waveguides and polarization-independent two-mode (de)multiplexer on thin film Lithium niobate. *Opt. Commun.* **2021**, *500*, 127334. [CrossRef]
30. Huang, W.; Luo, Y.; Zhang, W.; Li, C.; Li, L.; Yang, Z.; Xu, P. High-sensitivity refractive index sensor based on Ge–Sb–Se chalcogenide microring resonator. *Infrared Phys. Technol.* **2021**, *116*, 103792. [CrossRef]
31. Ding, Y.; Xu, J.; Da Ros, F.; Huang, B.; Ou, H.; Peucheret, C. On-chip two-mode division multiplexing using tapered directional coupler-based mode multiplexer and demultiplexer. *Opt. Express* **2013**, *21*, 10376–10382. [CrossRef] [PubMed]
32. Wang, Q.; He, Y.; Wang, H.; Wang, Z.; Shen, J.; Zhang, Y.; Su, Y. On-chip mode division (de)multiplexer for multi-band operation. *Opt. Express* **2022**, *30*, 22779–22787. [CrossRef] [PubMed]
33. Nath, J.P.; Dhingra, N.; Saxena, G.J.; Sharma, E.K. Compact Mode Division (de)Multiplexer Based on Collaterally Coupled SOI Waveguides. *IEEE Photonics Technol. Lett.* **2020**, *32*, 595–598. [CrossRef]
34. Huang, X.; Liu, Y.; Li, Z.; Fan, Z.; Han, W. High-performance and compact integrated photonics platform based on silicon rich nitride–lithium niobate on insulator. *APL Photonics* **2021**, *6*, 116102. [CrossRef]
35. Yin, M.; Deng, Q.; Li, Y.; Wang, X.; Li, H. Compact and broadband mode multiplexer and demultiplexer based on asymmetric plasmonic–dielectric coupling. *Appl. Opt.* **2014**, *53*, 6175–6180. [CrossRef]
36. Han, X.; Chen, L.; Jiang, Y.H.; Frigg, A.; Xiao, H.F.; Nguyen, T.G.; Boes, A.; Yang, J.H.; Ren, G.H.; Su, Y.K.; et al. Integrated Subwavelength Gratings on a Lithium Niobate on Insulator Platform for Mode and Polarization Manipulation. *Laser Photonics Rev.* **2022**, *16*, 2200130. [CrossRef]
37. Han, X.; Jiang, Y.H.; Xiao, H.F.; Yuan, M.R.; Nguyen, T.G.; Boes, A.; Ren, G.H.; Zhang, Y.; Hao, Q.F.; Su, Y.K.; et al. Subwavelength Grating-Assisted Contra-Directional Couplers in Lithium Niobate on Insulator. *Laser Photonics Rev.* **2023**, *17*, 2300203. [CrossRef]

Disclaimer/Publisher's Note: The statements, opinions and data contained in all publications are solely those of the individual author(s) and contributor(s) and not of MDPI and/or the editor(s). MDPI and/or the editor(s) disclaim responsibility for any injury to people or property resulting from any ideas, methods, instructions or products referred to in the content.